ACS APPLIED MATERIALS & INTERFACES

Research Article

www.acsami.org

# Improved Performance of $CuInS_2$ Quantum Dot-Sensitized Solar Cells Based on a Multilayered Architecture

Jia-Yaw Chang,* Jie-Mo Lin, Li-Fong Su, and Chia-Fu Chang

Department of Chemical Engineering, National Taiwan University of Science and Technology, Section 4, #43, Keelung Road, Taipei 106, Taiwan, Republic of China

Supporting Information

**ABSTRACT:** This Article describes a $CuInS_2$ quantum dot (QD)-sensitized solar cell (QDSSC) with a multilayered architecture and a cascaded energy-gap structure fabricated using a successive ionic-layer adsorption and reaction process. We initially used different metal chalcogenides as interfacial buffer layers to improve unmatched band alignments between the $TiO_2$ and $CuInS_2$ QD sensitizers. In this design, the photovoltaic performance, in terms of the short-circuit current density ($J_{SC}$), open-circuit voltage ($V_{OC}$), fill factor (FF), and power conversion efficiency (PCE), was significantly improved. Both $J_{SC}$ and $V_{OC}$ were improved in $CuInS_2$-based QDSSCs in the presence of interfacial buffer layers because of proper band alignment across the heterointerface and the negative band edge movement of $TiO_2$. The PCE of $CuInS_2$-based QDSSCs containing $In_2Se_3$ interfacial buffer layers was 1.35%, with $J_{SC}$ = 5.83 mA/cm$^2$, $V_{OC}$ = 595 mV, and FF = 39.0%. We also examined the use of alternative CdS and CdSe hybrid-sensitized layers, which were sequentially deposited onto the $In_2Se_3/CuInS_2$ configuration for creating favorable cascaded energy-gap structures. Both $J_{SC}$ (11.3 mA cm$^{-2}$) and FF (47.3%) for the $CuInS_2$/CdSe hybrid-sensitized cells were higher than those for $CuInS_2$-based cells ($J_{SC}$ = 5.83 mA cm$^{-2}$ and FF = 39.0%). In addition, the hybrid-sensitized cells had PCEs that were 1.3 times those of cells containing identically pretreated $In_2Se_3$ interfacial buffer layers. Additionally, we determined that ZnSe served as a good passivation layer on the surface of $CuInS_2$/CdSe hybrid-sensitized QDs, prevented current leakage from the QDs to electrolytes, and lowered interfacial charge recombination. Under simulated illumination (AM 1.5, 100 mW cm$^{-2}$), multilayered QDSSCs with distinct architectures delivered a maximum external quantum efficiency of 80% at 500 nm and a maximum PCE of 4.55%, approximately 9 times that of QDSSCs fabricated with pristine $CuInS_2$.

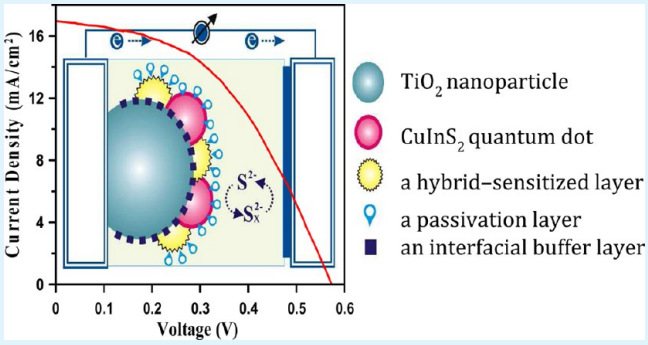


**KEYWORDS:** *quantum dot-sensitized solar cell, $CuInS_2$, multilayered architecture, solar energy*

## 1. INTRODUCTION

Dye-sensitized solar cells (DSSCs) are a promising renewable solar energy source because of their low cost, high durability, and low environmental impact.[1,2] Recently, semiconductor quantum dots (QDs) have also attracted significant interest as sensitizers in QD-sensitized solar cells (QDSSCs)[3] because they enable control of the tunable energy band gap by changing their size. In addition, QDs have higher extinction coefficients and enable multiple exciton generation from a single incident photon through the impact ionization effect.[4−6] It has been demonstrated that QDSSCs with an internal quantum efficiency of approximatly 100% can be prepared by utilizing 4-butylamine-capped QDs and $Li_2S$ elecytrolytes.[7] However, the power conversion efficiency (PCE) of QDSSCs is lower than that of DSSCs.

Interfacial tailoring, which can produce drastically different electron-transfer dynamics, has been shown to enhance the efficiency of photovoltaic devices. For instance, a hydrogenated, intrinsically amorphous a-Si/H($i$) interfacial layer has enabled a high open-circuit voltage in silicon heterojunction solar cells as a result of the layer's excellent passivating properties between amorphous and crystalline silicon (c-Si(n or p)).[8] In addition, poly(3,4-ethylene- dioxylenethiophene)/poly(styrenesulfonate) is often used as an interfacial layer between the photoactive layer and the indium tin oxide substrate to facilitate hole-collection/extraction and to enhance the overall efficiency of photovoltaic devices. CdS[9] and ZnS[10] buffer layers can be employed in the Cu(In,Ga)$Se_2$-based thin-film solar cells to protect the junction region from sputtering damage during subsequent zinc oxide deposition and to modify the surface of the Cu(In,Ga)$Se_2$ absorber. The cells exhibited efficiencies of 19.9 and 18.5% when the CdS[9] and ZnS[10] buffer layers were used, respectively.

In QDSSCs, substantial research has also been conducted to devise interfacial tailoring strategies that enhance the photovoltaic performance. For example, it has been reported that

Received: June 29, 2013
Accepted: August 12, 2013
Published: August 12, 2013

 © 2013 American Chemical Society 

molecular linkers (e.g., mercapropropionic acid[11,12] and benzenethiol derivatives[13−15]) are used to tether QDs to $TiO_2$, thereby allowing a uniform coverage, and they act as a molecular dipole to generate a more favorable energy-level alignment between QDs and $TiO_2$, leading to a significant increase in the energy conversion efficiency of QDSSCs. Similarly, Samadpour and co-workers[16] have adopted a fluorine treatment, which utilizes $NH_4F$ or HF on $TiO_2$ photoelectrode leads, to increase the QDSSC performance. Research has also recently been focused on the modification of the interface between $TiO_2$ and QDs through the insertion of an interfacial buffer layer in QDSSCs. For instance, both Im et al.[17] and Xu et al.[18] inserted ZnS interfacial layers between QD sensitizers and $TiO_2$ nanoparticles in QDSSCs, resulting in a PCE of 0.12−2.2%. Similarly, Hu et al.[19] used heat treatment and a CdS buffer layer to achieve a PCE of 1.47% in QDSSCs. In our previous work,[20] we increased the PCE by 73% by using a $Cu_2S$ buffer layer; the PCE in the $CuInS_2$ configuration is 0.52% and that in the $Cu_2S/CuInS_2$ configuration is 0.90%. In addition, the use of alternative sensitizers along with an initial QD sensitizer can broaden the absorption coverage of the solar spectrum and ensure efficient charge transfer in the heterointerface of hybrid sensitizers as compared to systems with a single sensitizer. Lin et al.[21] demonstrated that CdSe layers in CdS/CdSe photoanodes had longer photoluminescence lifetimes and higher PCEs as compared to CdSe/CdS photoanodes with CdSe layers. These hybrid-sensitized QDSSCs also had superior photocurrents, cell voltages, and overall efficiencies than those of single-sensitized QDs.[22−26] Previous research has also reported the use of wide-band-gap semiconductors (typically ZnS) as passivation layers on the surfaces of QD sensitizers with the aim of suppressing current leakage from the QDs to electrolytes and lowering interfacial charge recombination in QDSSCs.[27−34] Given this information, further research to understand optimal design and the use of various interfacial layers at the interface of the $TiO_2$/QD sensitizer/electrolyte is critical for maximizing efficient charge separation at the heterointerface and for improving the performance of QDSSCs.

In this study, we specifically used a $CuInS_2$ QD sensitizer in a QDSSC because of its band gap (Eg ≈ 1.5 eV) and high extinction coefficient ($\sim 10^5$ $cm^{-1}$) at 500 nm.[35] A schematic description of the system is presented in Scheme 1. We investigated the effects of using (1) metal chalcogenides as interfacial buffer layers in $TiO_2$ films sensitized with $CuInS_2$ QDs and (2) passivation layers of zinc chalcogenides with wide band gaps on the photovoltaic performance of QDSSCs (as shown in Scheme 1). Meanwhile, an alternative hybrid-sensitized layer was sequentially deposited onto a $CuInS_2$ QD, forming a favorable cascade hybrid-sensitized structure through the successive ionic layer adsorption and reaction (SILAR) method. To the best of our knowledge, the present work is the first attempt to incorporate an $In_2Se_3$ interfacial buffer layer and a CdSe hybrid-sensitizer into a $CuInS_2$-based QDSSC, yielding a PCE of 3.15%. Moreover, passivation with a ZnSe layer can further increase the QDSSC efficiency of the QDSSC to 4.55%. The incident photon-to-current conversion efficiency (IPCE) and electrochemical impedance spectra (EIS) were correlated to explain the efficacy of a $CuInS_2$-based QDSSC with a distinctive architecture.

**Scheme 1. Schematic Illustration of Multilayered QDSSCs Fabricated by Successively Depositing an Interfacial Buffer Layer, a $CuInS_2$ Sensitized QD, a Hybrid-Sensitizer Layer, and a Passivation Layer**

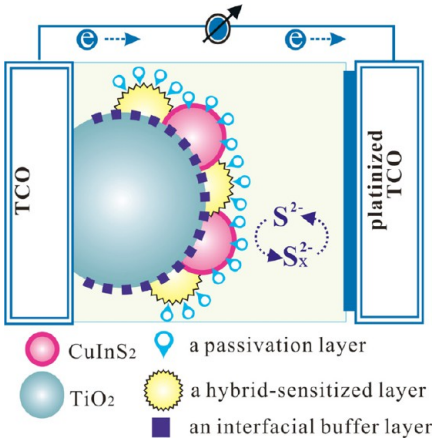


## 2. EXPERIMENTAL SECTION

**2.1. Materials.** Copper(II) nitrate hemipentahydrate ($Cu(NO_3)_2$, 98%) and selenium(IV) oxide ($SeO_2$, 99.4%) were purchased from Alfa-Aesar (Ward Hill, MA, USA). Sodium borohydride ($NaBH_4$, 98.0%), indium(III) nitrate hydrate ($In(NO_3)_3$, 99.9%), and sulfur powder (S, 99.98%) were purchased from Sigma-Aldrich (Milwaukee, WI, USA). Potassium chloride (99+%) and sodium sulfide nonhydrate ($Na_2S$, 98+%) were purchased from Acros Organics (Morris Plains, NJ, USA). Zinc acetate dihydrate ($ZnAc_2$, 99.8%) was obtained from J.T. Baker (Phillipsburg, NJ, USA). Cadmium nitrate ($Cd(NO_3)_2$, 99%) was obtained from Hayashi Pure Chemical Ind., Ltd. (Osaka, Japan). All chemicals were used directly without further purification.

**2.2. Device Fabrication.** *2.2.1. Preparation of the $TiO_2$ Electrode.* Prior to the fabrication of $TiO_2$ films, fluorine-doped tin oxide (FTO) glass was ultrasonically cleaned sequentially for 10 min each in detergent, water, 2-propanol, and acetone. Mesoscopic $TiO_2$ films were prepared by screen printing of a $TiO_2$ slurry (Solaronix, Ti-Nanoxide T/SP) on the FTO glass (TEC 7, Pilkington USA, with a sheet resistance of 8 Ω/square and thickness of 2.2 mm). A paste for the scattering layer containing anatase $TiO_2$ particles (Solaronix, Ti-Nanoxide R/SP) was deposited by screen printing, resulting in light-scattering $TiO_2$ films. This was followed by sintering at 500 °C for 30 min.

*2.2.2. Deposition of the Interfacial Buffer Layers on $TiO_2$ Photoanodes.* To deposit the metal chalcogenide interfacial buffer layer on $TiO_2$ electrodes, prepared $TiO_2$ electrodes were immersed for 1 min in a solution containing a $3 \times 10^{-2}$ M metal cations (e.g., $Cd(NO_3)_2$, $Cu(NO_3)_2$, or $In(NO_3)_3$) and methanol. We then rinsed the electrodes with methanol, immersed them for 1 min in a solution containing $3 \times 10^{-2}$ M sulfur or a selenium precursor, methanol, and water, and finally rinsed them again with methanol. The selenium precursor was synthesized by heating a mixture of $9 \times 10^{-4}$ mol $SeO_2$ in 25 mL ethanol and then reducing the mixture with $NaBH_4$ in ethanol according to a previously modified report.[36] The sulfur precursor was synthesized by adding 0.135 mol $Na_2S$ in a 50 mL solvent of methanol/water (7:3, v/v).

*2.2.3. Deposition of $CuInS_2$ Sensitizers on $TiO_2$ Photoanodes.* We then exposed $TiO_2$ photoanodes containing interfacial buffer layers to three different solutions: (1) 0.10 M $In(NO_3)_3$ in methanol for 1 min, (2) $1.25 \times 10^{-3}$ M $Cu(NO_3)_2$ in methanol for 0.5 min, and (3) 0.135 M $Na_2S$ in a 50 mL solvent of methanol/water (7:3, v/v) for 4 min. In between each immersion, the electrodes were rinsed with pure methanol and dried with nitrogen gas. This procedure constituted a complete SILAR cycle that was repeated for six cycles until the desired $CuInS_2$-based $TiO_2$ photoanodes containing the appropriate interfacial buffer layers were created.

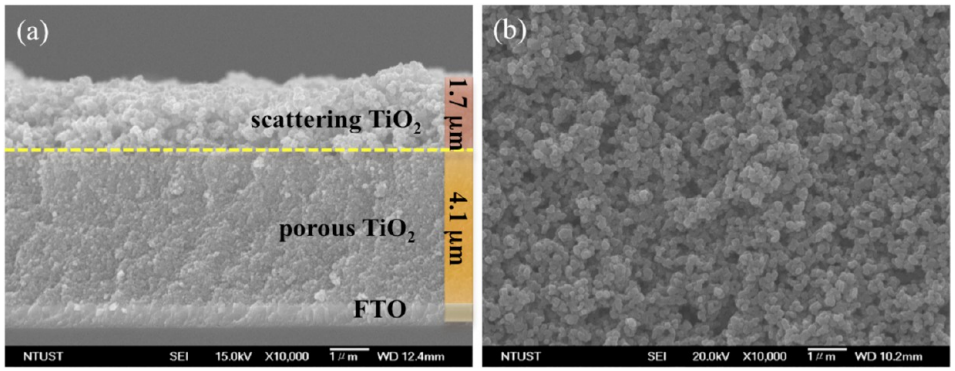


**Figure 1.** (a) Cross-section and (b) top view of the SEM image of a $TiO_2$ electrode composed of porous $TiO_2$ and light-scattering $TiO_2$.

*2.2.4. Deposition of Hybrid Sensitizers on $CuInS_2$-Based $TiO_2$ Photoanodes Containing $In_2Se_3$ Interfacial Buffer Layers.* For the deposition of CdS hybrid-sensitized layers, $CuInS_2$-based $TiO_2$ photoanodes containing $In_2Se_3$ interfacial buffer layers were consecutively immersed in two different solutions for 1 min containing (1) 0.1 M $Cd(NO_3)_2$ in methanol and (2) 0.1 M $Na_2S$ in a 50 mL solvent of methanol/water (7:3, v/v). In between immersions, the electrodes were rinsed with pure methanol and dried with nitrogen gas. This procedure constituted a complete SILAR cycle that was repeated for several cycles (between two and four) until the desired $CuInS_2$/CdS hybrid-sensitized $TiO_2$ photoanodes containing $In_2Se_3$ interfacial buffer layers were created. For the deposition of the CdSe hybrid-sensitized layers, $CuInS_2$-based $TiO_2$ photoanodes containing $In_2Se_3$ interfacial buffer layers were consecutively immersed for 1 min each in two different solutions containing (1) 0.1 M $Cd(NO_3)_2$ in methanol and (2) 0.1 M selenium precursor. In between each immersion, the electrodes were rinsed with pure methanol and dried with nitrogen gas. This SILAR process was repeated for several cycles (between two and four) until the desired $CuInS_2$/CdSe hybrid-sensitized $TiO_2$ photoanodes containing $In_2Se_3$ interfacial buffer layers were created.

*2.2.5. Deposition of ZnS or ZnSe Passivation Layers on $CuInS_2$/CdSe Hybrid-Sensitized $TiO_2$ Photoanodes Containing $In_2Se_3$ Interfacial Buffer Layers.* For the deposition of ZnS passivation layers, $CuInS_2$/CdSe hybrid-sensitized $TiO_2$ photoanodes containing $In_2Se_3$ interfacial buffer layers were consecutively immersed for 1 min in solutions containing (1) 0.1 M $ZnAc_2$ in methanol and (2) 0.1 M $Na_2S$ in a 50 mL solvent of methanol/water (7:3, v/v). In between each immersion, the electrodes were rinsed with pure methanol and dried with nitrogen gas. This SILAR process was repeated for two cycles. For the deposition of ZnSe passivation layers, $CuInS_2$/CdSe hybrid-sensitized $TiO_2$ photoanodes containing $In_2Se_3$ interfacial buffer layers were consecutively immersed for 1 min in solutions containing (1) 0.1 M $ZnAc_2$ in methanol and (2) 0.1 M selenium precursor. Between immersions, the electrodes were rinsed with pure methanol and dried with nitrogen gas. This SILAR process was repeated for two cycles.

*2.2.6. Fabrication of QDSSCs.* After preparing the QD-sensitized $TiO_2$ photoanodes by the SILAR process described above, the solar cells were assembled into a sandwich-type configuration by placing a platinum-deposited conducting glass (counter electrode) prepared by sputter deposition on the QD-sensitized $TiO_2$ photoanodes by using a 60 $\mu$m-thick Surlyn sheet (DuPont 1702) as a spacer. Sputtering was carried out in a JEOL JCF-1300 sputtering system. The polysulfide redox electrolyte consisting of 1.8 M $Na_2S$, 2.0 M sulfur, and 0.2 M potassium chloride in a mixture of methanol/water (3:7, v/v) was introduced into the sealed cell by the capillary effect.

**2.3. Sample Characterization.** Field emission scanning electron microscopy (SEM) was performed on a JEOL 6335F (JEOL USA Inc., USA) equipped with an energy dispersive X-ray (EDS) analyzer. TEM imaging was carried out on Philips Tecnai G2 F20 microscope (Philips, Holland) operated at an accelerating voltage of 200 kV. UV–vis–near-infrared (NIR) absorption spectra were measured with a JASCO V-670 spectrometer. X-ray photoelectron spectroscopy (XPS) was performed using an ESCALAB 250 photoelectron spectrometer (Thermo VG Scientific, West Sussex, UK) with Al K$\alpha$ (1486 eV) excitation. The chemical shifts of the XPS peaks were standardized with respect to the C 1s peak at 284.6 eV. The photocurrent density–photovoltage characteristics of the QDSSC were recorded under the illumination provided by a solar simulator (Oriel 6691 450 W xenon arc lamp, CT, USA) at 100% sunlight (AM 1.5, 100 mW $cm^{-2}$). The incident light intensity was calibrated with a NREL standard Si solar cell. The IPCE plotted as a function of the excitation wavelength was measured with a PEC-S20 instrument (Peccell Technologies, Inc., Kanagawa, Japan). A metal mask defined the cell active area to be 0.16 $cm^2$. To analyze the electron behaviors in QDSSCs, EIS were measured using an impedance analyzer (PGSTAT 302N, Autolab, Eco-Chemie, The Netherlands) in the dark at −0.6 V bias, with the magnitude and frequency of the alternative signal being 10 mV and $10^{-1}$–$10^5$ Hz, respectively. Impedance spectra were analyzed using an equivalent circuit model, and the model parameters were obtained by Nova software.

## 3. RESULTS AND DISCUSSION

**3.1. Performance of the Interfacial Buffer Layers.** The SEM image (Figure 1) shows a $TiO_2$ electrode that contains a porous nanocrystalline film (~4.1 $\mu$m thickness) as the sensitizer absorption layer at the bottom as well as a larger nanocrystalline film (~1.7 $\mu$m thickness) on top for light scattering. We pretreated the surfaces of bare $TiO_2$ film-modified electrodes by soaking them in an aqueous solution containing metal cations and chalcogenide anions to create an interfacial buffer layer before the deposition of $CuInS_2$ QDs. Pretreated $TiO_2$ electrodes were further sensitized with $CuInS_2$ QDs prepared through six cycles of SILAR deposition, which involved successive immersion of $TiO_2$ electrodes in cation/anion solutions to deposit the $CuInS_2$ QDs as photoanodes on the $TiO_2$ surfaces. Within this set up, $TiO_2$ acted as a semiconductor with a band gap energy of 3.0–3.2 eV and served as an electron acceptor. In addition, $CuInS_2$ QDs served as both light harvesters and electron donors. The heterojunction provided a system for energy harvest and electron transport in the photoelectrode. The photoelectrode was joined to a counter electrode, which is a TCO glass activated with a platinum catalyst, followed by the injection of sulfide/polysulfide ($S^{2-}/S_x^{2-}$) electrolytes that assisted in the regeneration of the $CuInS_2$ QD by scavenging the holes.

We measured the photovoltaic performance under illumination from a solar simulator at 1 sun (AM 1.5, 100 mW $cm^{-2}$). The characteristic current–voltage ($J$–$V$) curves and PCE percentage enhancement of the QDSSCs are given in Figure 2a, and the relations between the photovoltaic parameters and the

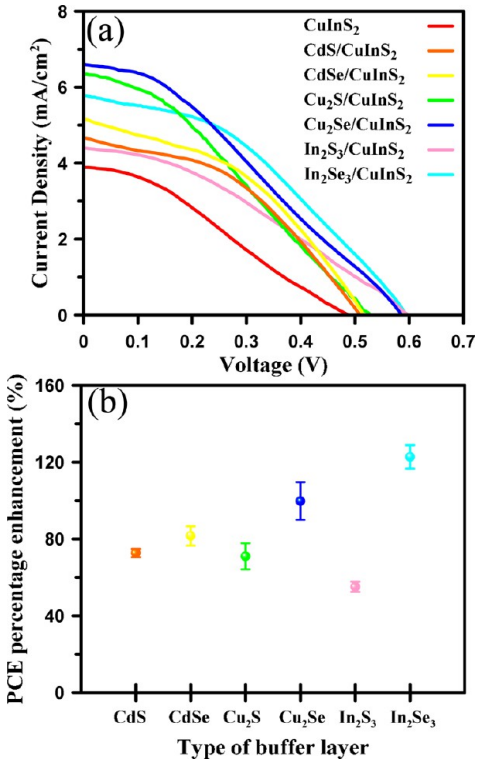


**Figure 2.** (a) Photocurrent density–voltage characteristic curves and (b) PCE percentage enhancement of $CuInS_2$-based QDSSCs containing different interfacial buffer layers of metal chalcogenide. Data are reported as the mean values of three replicates ± standard deviation.

short-circuit current density ($J_{SC}$), open-circuit voltage ($V_{OC}$), fill factor (FF), and PCE are summarized in Table 1. We found

**Table 1. Summary of the Photovoltaic Properties of $CuInS_2$-Based QDSSCs Fabricated with a Different Interfacial Buffer Layer of Metal Chalcogenide**

| sample | $J_{SC}$ (mA cm$^{-2}$) | $V_{OC}$ (mV) | FF (%) | PCE (%) |
|---|---|---|---|---|
| $CuInS_2$ | 3.91 | 484.9 | 30.5 | 0.58 |
| $CdS/CuInS_2$ | 4.65 | 510.1 | 42.6 | 1.01 |
| $CdSe/CuInS_2$ | 5.18 | 520.0 | 41.1 | 1.11 |
| $Cu_2S/CuInS_2$ | 6.34 | 530.0 | 31.5 | 1.06 |
| $Cu_2Se/CuInS_2$ | 6.53 | 585.1 | 31.9 | 1.22 |
| $In_2S_3/CuInS_2$ | 4.42 | 594.8 | 34.0 | 0.89 |
| $In_2Se_3/CuInS_2$ | 5.83 | 595.0 | 39.0 | 1.35 |

that the $J_{SC}$, $V_{OC}$, and FF of the QDSSCs with pristine $CuInS_2$ QDs were 3.91 mA cm$^{-1}$, 484.9 mV, and 30.5%, respectively, resulting in a PCE of 0.58%. In addition, $J_{SC}$, $V_{OC}$, and FF were higher for $CuInS_2$-based QDSSCs with interfacial buffer layers compared to pristine $CuInS_2$-based QDSSCs. Thus, we assert that interfacial buffer layers enhanced the overall conversion efficiency of the cells and played important roles in improving the photovoltaic performance. As shown by the data given in Table 1, the $V_{OC}$ value for the $CuInS_2$-based QDSSCs with interfacial buffer layers was significantly enhanced compared to that for pristine $CuInS_2$-based QDSSCs. In principle, $V_{OC}$ is determined by the potential difference between the Fermi energy level that is close to the conduction band edge position and the redox potential of the electrolyte. Therefore, it can be inferred that the pretreated interfacial buffer layers assisted in electron accumulation within the $TiO_2$ photoanode, causing the Fermi-level shift of $TiO_2$ toward more negative potentials, resulting in the higher photovoltage. The improvement in $J_{SC}$ for QDSSCs with interfacial buffer layers was probably related to their ability to transfer charge from the $CuInS_2$ QDs to the $TiO_2$ NPs through the pretreated interfacial buffer layer. Similar to the case of chalcopyrite solar cells, the interfacial buffer layer, composed of metal chalcogenides (e.g., CdS, $In_2S_3$, and ZnS),[37] separated the I-III-VI absorber layer and the transparent front electrode and could be used to control interfacial properties. This feature resulted in an appropriate charge density and Fermi-level position at the interface. In particular, the proper band alignment strongly affected the charge transfer across the buffer layer/chalcopyrite interface. For example, photovoltaic devices consisting of p-type $Cu(In,Ga)Se_2$ absorbers with $In_x(OOH,S)_y$[38] buffer layers yielded a 12.55% conversion efficiency as the result of unfavorable conduction-band alignment at the heterojunction. However, the same photovoltaic devices with CdS[39] buffer layers achieved an efficiency of more than 19%. Loef et al. also demonstrated that thin interfacial n-type buffer layers between n-type $TiO_2$ and p-type $CuInS_2$ have donor densities of $2 \times 10^{17}$ cm$^{-3}$ at 400 K, which was higher than the effective acceptor density of $4 \times 10^{16}$ cm$^{-3}$ at 400 K in the absence of buffer layers.[40]

$CuInS_2$-based QDSSCs using $In_2Se_3$ as the interfacial buffer layer exhibited an optimum overall performance; $J_{SC}$ increased from 3.91 to 5.83 mA cm$^{-2}$, $V_{OC}$ increased from 484.9 to 595.0 mV, FF increased from 30.5 to 39.0%, and PCE increased from 0.58 to 1.35% (i.e., an overall efficiency increase of 130%) in comparison to pristine $CuInS_2$-based QDSSCs lacking interfacial buffer layers (Table 1). We suggest several possible explanations for the performance enhancement of QDSSCs that incorporate pretreated $In_2Se_3$ interfacial buffer layers. First, band alignment in QDSSCs with buffer layers may have provided more favorable conditions for carrier migration from the conduction bands of chalcopyrite $CuInS_2$ toward the conduction bands of anatase $TiO_2$ through $In_2Se_3$ interfacial buffer layers. A similar performance enhancement of a QDSSC photovoltaic device has been reported previously by Hu et al.[19] who used CdS as a buffer layer to tune the band alignment between $CuInS_2$ and $TiO_2$. This enhancement led to increases of 1.47 and 300% in PCE and cell performance, respectively, as compared to a $CuInS_2$ reference sample. Wienke et al.[41] also reported that electronic contact between $CuInS_2$ and $TiO_2$ was significantly improved if a barrier film was deposited prior to $CuInS_2$ deposition. Another possible explanation of the performance enhancement is that the formation of $CuInSe_xS_{1-x}$ hybrid-sensitized interlayers, which are beneficial for light-harvesting capacity and photovoltaic performance, occurred via cation-exchange reactions between the $In_2Se_3/CuInS_2$ heterointerface. This exchange was possible because $Cu^+$ and $In^{3+}$ ions have similar ionic radii (60–62 pm). Cation-exchange reactions usually take place in aqueous solutions containing the respective salt precursors, and these reactions have previously been applied to the synthesis of various metal chalcogenide nanostructures.[42−47] We found that the enhancements in the average PCE for $CuInS_2$ QDSSCs containing metal selenide-based buffer layers were higher than those containing metal sulfide-based buffer layers (Figure 2b). Figure S1 in the Supporting Information shows the average PCE of $CuInS_2$-based QDSSCs containing different interfacial buffer layers of metal chalcogenide. This result also suggests that the $CuInSe_xS_{1-x}$ hybrid-sensitized interlayers were formed by

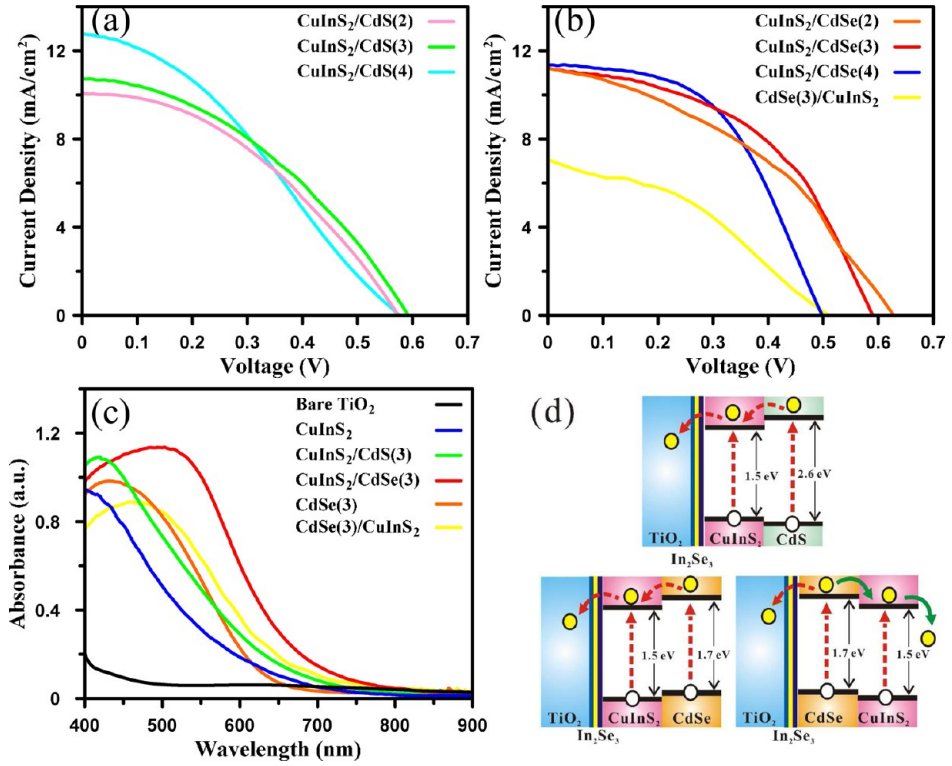


**Figure 3.** Photocurrent density–voltage characteristic curves for $CuInS_2$-based QDSSCs that contained $In_2Se_3$ interfacial buffer layers and were hybrid sensitized with different numbers of (a) CdS and (b) CdSe SILAR cycles under the illumination of a solar simulator at 1 sun (AM 1.5, 100 mW $cm^{-2}$). A sample after $m$ cycles of hybrid-sensitized QD deposition was denoted as $CuInS_2$/CdS($m$) or $CuInS_2$/CdSe($m$). (c) UV–vis absorption spectra of $CuInS_2$-, CdSe-, $CuInS_2$/CdS(3)-, $CuInS_2$/CdSe(3)-, and CdSe(3)/$CuInS_2$-sensitized photoanodes in the presence of an $In_2Se_3$ interfacial buffer layer as well as the bare $TiO_2$ electrode used as a reference. (d) Schematic energy-level diagram of $CuInS_2$/CdS (top layer), $CuInS_2$/CdSe (left side, bottom layer), and CdSe/$CuInS_2$ (right side, bottom layer) after band alignment when the adjoining semiconductors made contact. Orange and green arrows indicate the direction of carrier migration to $TiO_2$ and of carrier leakage to the electrolyte, respectively, after light illumination.

cation-exchange reactions when exposed to excess cations. Finally, we could attribute our results to the favorable relative orientations of $In_2Se_3$ interfacial planes, which are expected to occur at the heterogeneous interface between $TiO_2$ and $CuInS_2$. The $In_2Se_3$ structure is a layered structure consisting of [Se–In–Se–In–Se] sheets stacked together through Se-atom interactions along the $c$ axis, leaving one third of the indium atom sites empty and allowing weak interlayer van der Waals interactions.[48,49] $In_2Se_3$ compounds usually crystallize in a hexagonal structure with the $P6_3$ space group (lattice parameters $a = b = 0.4016$ nm and $c = 1.9222$ nm) and form quasi-two-dimensional flakes or platelets. Therefore, a layer-by-layer epitaxial growth of $In_2Se_3$ nanolayers can be easily achieved on the surface of $TiO_2$ substrates. According to classical nucleation theory,[35] the activation-energy barrier for the growth of an exterior material on pre-existing seeds in a solution is considerably lower than that for the independent generation of free-standing crystalline embryos.[36] $CuInS_2$ grows preferentially on the $In_2Se_3$ layer by SILAR rather than by forming separate nuclei in a solution because the activation energy for heterogeneous nucleation is much lower than that for homogeneous nucleation. Similar phenomena have been reported previously; CdS layers have been employed as seed layers that enhanced CdSe growth rates in QDSSCs.[50] Lee et al.[30] also reported that an ex situ synthesized CdS QD served as a seed layer on the mesoporous $TiO_2$ film and induced the nucleation and growth of CdSe QD in the QDSSC, significantly improving the efficiency of the cell with the seed layer.

### 3.2. Performance of CdS and CdSe Hybrid Sensitizers.

Although previous efforts have been made to increase light absorption using QD sensitizers, there is currently no single QD type that exhibits high absorption covering a wide range of visible and IR spectra. Hence, QDs with complementary light harvest capacities have been combined in an attempt to achieve broad-range absorption. From recent studies on hybrid-sensitized QDSSCs,[22−26] it has been concluded that QDSSCs with hybrid-sensitized structures (i.e., combined QDs) show greatly enhanced photovoltaic performance than those with a single QD. This enhancement in photovoltaic performance occurs as a result of the complementary effects in light harvest and the staircase band alignment at the hybrid-sensitizer interface, which facilitates charge transfer.

Therefore, to improve further the efficiency of $CuInS_2$-based QDSSCs containing $In_2Se_3$ interfacial buffer layers, tailoring alternative sensitizers on the surface of the initial QDs could provide a complementary light harvest capacity and result in energetically more favorable interfacial electron transfer. Among the QD sensitizers reported in the literature,[51−54] a higher band gap in CdS (2.6 eV in bulk) or CdSe (1.7 eV in bulk) semiconductors can cover different absorption ranges compared to that of $CuInS_2$ (1.5 eV in bulk) semiconductors. Thus, we used CdS and CdSe QDs as secondary sensitizers in our system. CdS or CdSe QDs were deposited along with $CuInS_2$ QDs on $TiO_2$ photoelectrodes using the SILAR process; these CdS or CdSe QDs act as light hybrid sensitizers.


dx.doi.org/10.1021/am402547e | ACS Appl. Mater. Interfaces 2013, 5, 8740−8752

The characteristic $J-V$ curves of $CuInS_2$ QDSSCs with CdS or CdSe hybrid-sensitizers and various SILAR cycles are shown in Figure 3a,b, and the $J_{SC}$, $V_{OC}$, FF, and PCE corresponding to the photovoltaic parameters are summarized in Table 2. The

**Table 2. Summary of the Photovoltaic Properties of $CuInS_2$-Based QDSSC Fabricated with Different Hybrid-Sensitized and Passivation Layers in the Presence of an $In_2Se_3$ Interfacial Buffer Layer**

| sample | $J_{SC}$ (mA cm$^{-2}$) | $V_{OC}$ (mV) | FF (%) | PCE (%) |
|---|---|---|---|---|
| $CuInS_2$/CdS(2) | 10.2 | 575.0 | 40.4 | 2.37 |
| $CuInS_2$/CdS(3) | 10.8 | 590.0 | 40.0 | 2.55 |
| $CuInS_2$/CdS(4) | 12.9 | 575.0 | 33.1 | 2.45 |
| $CuInS_2$/CdSe(2) | 11.3 | 625.0 | 40.5 | 2.86 |
| $CuInS_2$/CdSe(3) | 11.3 | 590.1 | 47.3 | 3.15 |
| $CuInS_2$/CdSe(4) | 11.2 | 500.0 | 51.4 | 2.89 |
| CdSe(3)/$CuInS_2$ | 7.09 | 515.0 | 37.2 | 1.36 |
| $CuInS_2$/CdSe(3)/ZnS | 14.6 | 610.0 | 36.9 | 3.27 |
| $CuInS_2$/CdSe(3)/ZnSe | 17.0 | 575.0 | 46.5 | 4.55 |

QDSSCs with CdS hybrid sensitizers additionally deposited on the surface of $CuInS_2$ photoanodes were compared with pristine $CuInS_2$-based QDSSCs, and this deposition was found to cause significant increases in $J_{SC}$ (5.83 to 10.8 mA cm$^{-2}$) over three CdS SILAR cycles, yielding a 200% increase in the overall efficiency (from 1.35 to 2.55%). The enhanced $J_{SC}$ resulted from the beneficial light-harvesting enhancement over the UV−vis spectrum from QDSSCs containing hybrid-sensitized CdS QDs (Figure 3c). Figure 3c presents the absorption spectra of $In_2Se_3$/$CuInS_2$, $In_2Se_3$/$CuInS_2$/CdS(3), and bare $TiO_2$ electrodes used for reference during UV−vis measurement. $In_2Se_3$/$CuInS_2$ photoanodes had absorption bands in the range of 400−700 nm. This broad range was attributed to the intrinsic properties of semiconductor QDs, which have continuous absorption spectra, and the molar extinction coefficients of QDs, which gradually increase toward shorter wavelengths. The UV−vis spectrum of $CuInS_2$/CdS(3) photoanodes showed a higher absorption intensity than $CuInS_2$ photoanodes (Figure 3c), indicating that cosensitization was beneficial for the light-harvesting capacity under identical pretreatments of $In_2Se_3$ interfacial buffer layers. In addition, it is also possible that the band position formed a cascade structure when $CuInS_2$ and CdS made contact. Schematic diagrams of the band alignment between $CuInS_2$ and CdS are shown in Figure 3d (top layer) for reference. Another possible explanation for the $J_{SC}$ enhancement is that a wide-band-gap CdS passivated the surface of $CuInS_2$ QDs to prevent the leakage of current. The dark current curves in Figure 3b confirm that $CuInS_2$/CdS(3) hybrid-sensitized QDSSCs have higher onset potentials than $CuInS_2$-based QDSSCs, demonstrating that interfacial recombination of the injected electrons from $TiO_2$ to electrolytes was inhibited by the high potential barrier of the CdS.

We observed the optimum performance from $CuInS_2$/CdSe(3) hybrid-sensitized QDSSCs containing $In_2Se_3$ interfacial buffer layers (Table 2 and Figure 3b). Both the $J_{SC}$ and FF values for the $CuInS_2$/CdSe(3) hybrid-sensitized cells (11.3 mA cm$^{-2}$ and 47.3%, respectively) were higher than those for $CuInS_2$-based cells (5.83 mA cm$^{-2}$ and 39.0%, respectively) because the PCE of the former system (3.15%) was 1.3 times that of the latter (1.35%). However, $V_{OC}$ continuously decreased as the number of CdSe SILAR cycles increased. Generally, the $V_{OC}$ of a solar cell can be attributed to the energy-level difference between the quasi-Fermi level of $TiO_2$ at the anode and the redox potential of electrolytes at the cathode. As a result, the drop in $V_{OC}$ with the increase in the number of CdSe SILAR cycles was attributed to excessive QD deposition, which caused clogging of the mesoporous $TiO_2$ film and resulted in the low diffusion efficiency of polysulfide electrolytes into the mesoporous $TiO_2$ film. The FF of $CuInS_2$/CdSe(3) hybrid-sensitized QDSSCs was greater than that of pristine $CuInS_2$-based QDSSCs, indicating that hybrid-sensitized QDSSCs were better able to inhibit charge recombination at the $TiO_2$/electrolyte interface because of the high QD coverage of the $TiO_2$ film. In addition, we attributed the $J_{SC}$ improvement to the enhanced light-harvesting capacity resulting from the extended light-absorption range of $CuInS_2$ and CdSe hybrid sensitizers. The absorption edge of $CuInS_2$/CdSe(3) photoanodes was significantly red shifted, and the absorbance intensity of these photoanodes was much greater than that of $CuInS_2$/CdS(3) and $CuInS_2$ photoanodes in the wavelength range of 450−800 nm (Figure 3c).

We also speculate that the improved performance of $CuInS_2$ and CdSe hybrid-sensitized QDSSCs was related to the cascade band structure formed in these systems. The schematic diagrams of band alignment are shown in Figure 3d as reference. The combination of $CuInS_2$ and CdSe semiconductor materials allowed for the redistribution of electrons in the $CuInS_2$/CdSe heterojunction via Fermi-level alignment, thereby inducing downward and upward shifts of conduction band edges for $CuInS_2$ and CdSe, respectively. This produced favorable cascaded energy-gap structures, which provided an adequate driving force for the increased amount of electron injection from QD sensitizers into the $TiO_2$. As shown in Figure 4a, the IPCE curve of the $CuInS_2$/CdSe(3)-based QDSSCs exhibited a broad spectrum with a maximum value of 52% at 485 nm and extended the photo absorption to a wider visible region (750 nm). However, when the QDSSC was fabricated with a CdSe(3)/$CuInS_2$ inverted cascade structure, it caused the consumption of the photogenerated electron (i.e., "electron leakage") from the conduction band of the CdSe QDs to the $CuInS_2$ QDs, as shown in Figure 3d (right side, bottom layer). As a result, $J_{SC}$, $V_{OC}$, and FF for CdSe(3)/$CuInS_2$ inverted hybrid-sensitized QDSSCs were found to be significantly less than those for the reference $CuInS_2$/CdSe(3) hybrid-sensitized QDSSCs by 37% (from 11.3 to 7.09 mA cm$^{-2}$), 13% (from 590 to 515 mV), and 21% (from 47.3 to 37.2%), respectively (Table 2 and Figure 3b). These results are also consistent with previous reports that indicated that inverting the order of the hybrid sensitizers in QDSSCs resulted in decreased cell performance.[55]

Furthermore, the IPCE of CdSe(3)/$CuInS_2$ inverted hybrid-sensitized QDSSCs was lower than that of $CuInS_2$/CdS(3) and $CuInS_2$/CdSe(3) hybrid-sensitized QDSSCs across the visible spectrum (Figure 4a), which is consistent with the corresponding current density by the $J-V$ characteristics of the cell in Figure 3, panels a and b. The poor IPCE results for CdSe(3)/$CuInS_2$ inverted hybrid-sensitized QDSSCs were probably the result of lower light-harvesting and electron-injecting capacities, suggesting that electrons from $CuInS_2$ could not be efficiently transferred to the higher conduction band of CdSe because of unfavorable band alignment in the inverted cascade structure (CdSe/$CuInS_2$). As shown in Figure 3c, the absorption intensity of CdSe(3)/$CuInS_2$ photoanodes became weaker

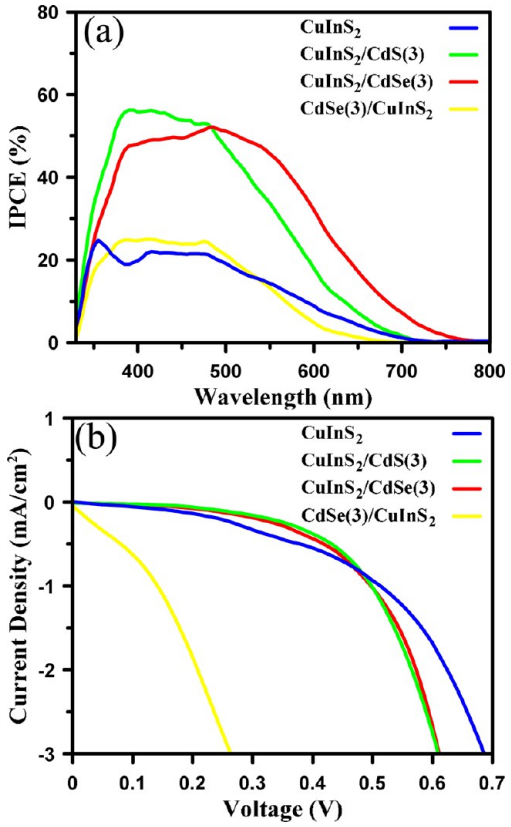


**Figure 4.** (a) IPCE of a $CuInS_2$-based QDSSC that contained an $In_2Se_3$ interfacial buffer layer and was hybrid sensitized with CdS and CdSe by three SILAR deposition cycles. (b) Photocurrent density–voltage characteristics of the corresponding cells measured under dark conditions.

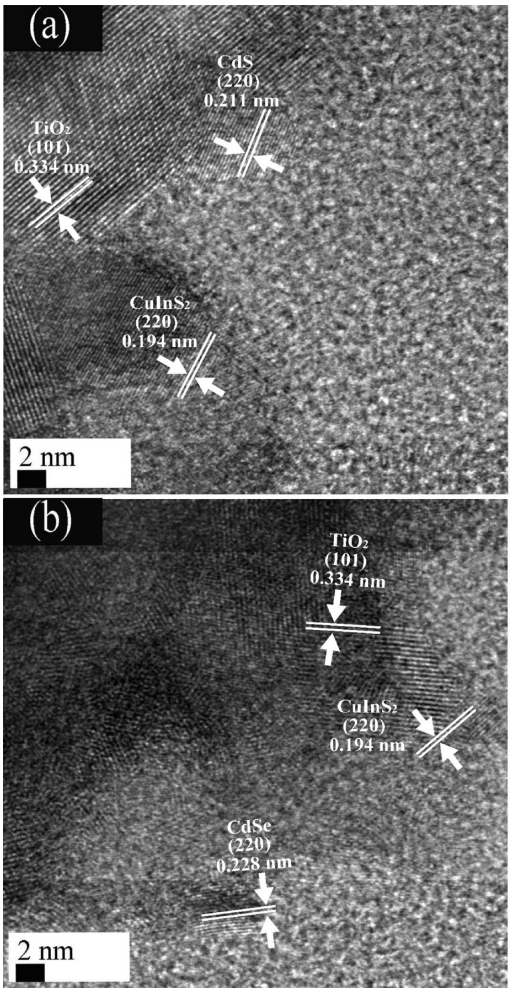


**Figure 5.** High-resolution TEM images of (a) $CuInS_2$/CdS(3) and (b) $CuInS_2$/CdSe(3) hybrid sensitized on a $TiO_2$ photoelectrode.

with an absorption maximum of around 500 nm; however, the shape of the spectrum remained roughly equivalent to that of $In_2Se_3$/$CuInS_2$/CdSe(3) photoanodes. To exclude the absorption of $CuInS_2$, we observed CdSe photoanodes separately without the incorporation of $CuInS_2$. With this approach, we noted a maximum absorption for CdSe photoanodes of approximately 450 nm and an absorption edge that was blue shifted to 650 nm. Accordingly, we propose that CdSe(3)/$CuInS_2$ inverted hybrid-sensitized structures significantly altered their electronic absorption structure and light-harvesting efficiency compared to $CuInS_2$/CdSe(3) original hybrid-sensitized structures. This result is supported by the $J$–$V$ characteristics of cells with electrodes measured under dark conditions (Figure 4b). The dark current curves confirmed that CdSe(3)/$CuInS_2$ samples had the lowest onset potential and high current leakage. However, a dark current onset for $CuInS_2$/CdSe(3) hybrid-sensitized QDSSCs occurred at higher voltages than that in the case of $CuInS_2$-based QDSSCs, suggesting that the CdSe coating on $CuInS_2$ QDs prevented dark current and led to higher $J_{SC}$.

Analysis of the products by high-resolution TEM revealed the coexistence of $CuInS_2$ and CdS QDs on the $TiO_2$ film (Figure 5a). The existence of well-resolved lattice planes demonstrated the presence of nanocrystals with discriminable lattice spacing of 0.194 and 0.211 nm, which is close to the interplanar spacing of the (220) lattice planes of $CuInS_2$ (JCPDS card no. 85-1575) and CdS (JCPDS card no. 41-1049), respectively. We found that the resulting sample was composed of copper, indium, sulfur, and cadmium elements using EDS measurements (Figure S2a in the Supporting Information). The Au peaks are due to the gold TEM grid used in the measurement, and the Ti peaks originate from the $TiO_2$ nanocrystals. For $CuInS_2$/CdSe hybrid-sensitized QDSSCs, high-resolution TEM of QDs (Figure 5b) exhibited clear lattice fringes, which could be indexed to the (220) plane of the chalcopyrite $CuInS_2$ structure (JCPDS card no. 85-1575) and the (220) plane of the zinc-blende CdSe structure (JCPDS card no. 19-0191). The EDS analysis of this sample in the TEM image indicated the presence of copper, indium, sulfur, cadmium, and selenium elements (Figure S2b in the Supporting Information). This analysis was used to provide complementary information with the existence of well-resolved lattice planes of QD obtained in high-resolution TEM image.

**3.3. Performance Comparison of ZnS and ZnSe Passivation Layers in $CuInS_2$/CdSe Hybrid-Sensitized QDSSCs.** We expected that the high surface-to-volume ratio of QDs would significantly affect their structural and optical properties. Because defects on the surface of QDs serve as temporary "surface traps" for electrons, they hinder charge transfer into $TiO_2$ conduction bands and therefore greatly reduce PCE in QDSSCs. It has been reported that passivating a wide-band-gap shell on bare QDs can suppress the recombination of injected electrons at the photoanode/electrolyte interface and enhance the efficiency of QDSSCs.[13,29,32,34,56,57] Among the wide-gap semiconductors, zinc chalcogenide is a

direct wide-band-gap compound semiconductor with a bulk band gap of 1.21−3.7 eV. In this study, we used ZnSe and ZnS passivation layers in $CuInS_2$/CdSe(3) hybrid-sensitized QDSSCs with $In_2Se_3$ interfacial buffer layers.

After the deposition of ZnS passivation layers onto $CuInS_2$/CdSe(3) hybrid-sensitized QDSSCs, we observed that both $J_{SC}$ and $V_{OC}$ for $CuInS_2$/CdSe(3) hybrid-sensitized QDSSCs increased by approximately 29% (from 11.3 to 14.6 mA $cm^{-2}$) and 3% (from 590 to 610 mV), respectively (Table 2 and Figure 6a). We also determined that after this deposition

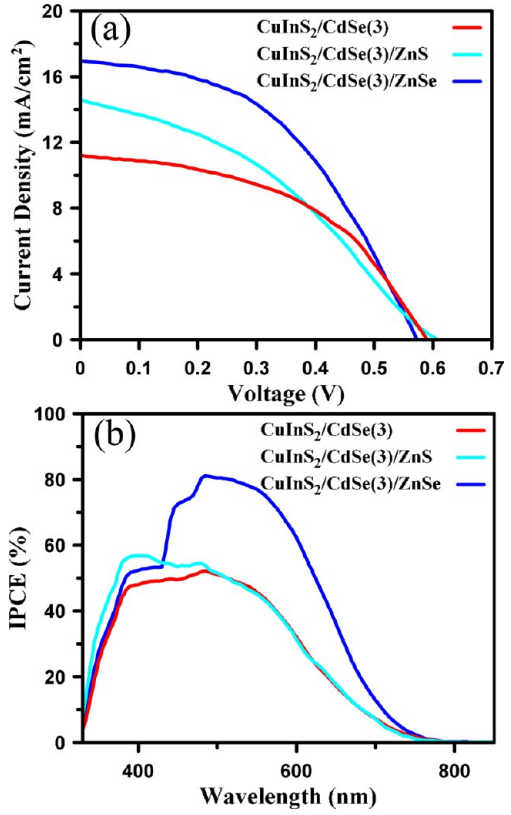


**Figure 6.** (a) Photocurrent density−voltage characteristics and (b) the IPCE of a $CuInS_2$/CdSe(3) hybrid-sensitized QDSSC coated with a ZnS and ZnSe passivation layer in the presence of an $In_2Se_3$ interfacial buffer layer.

the $CuInS_2$/CdSe/ZnS configuration had a lower FF, decreasing by 22% (from 47.3 to 36.9%). The FF of the $CuInS_2$/CdSe(3)/ZnS configuration was smaller than that of the $CuInS_2$/CdSe(3) or $CuInS_2$/CdSe(3)/ZnSe configuration, presumably because of the low driving force for electron regeneration. Photoexcited electrons in $CuInS_2$ and CdSe were easily injected into $TiO_2$ in the presence of a ZnS passivation layer, preventing current leakage from the QDs to the electrolytes. However, photogenerated holes in the valence band of QDs were not easily eliminated by $S^{2-}/S_x^{2-}$ electrolytes because the wider offsets in the valence band between the ZnS−$CuInS_2$ or ZnS−CdSe interface created a barrier for hole scavenging. As a result, a higher resistance in charge regeneration occurred in $CuInS_2$ and led to a smaller FF.

Compared to $CuInS_2$/CdSe(3) hybrid-sensitized QDSSCs, the $CuInS_2$/CdSe(3)/ZnSe configuration created a high photocurrent density of 17.0 mA $cm^{-2}$, which was 50% higher than that of QDSSCs lacking a passivation layer. Resultantly, the PCE for the $CuInS_2$/CdSe(3)/ZnSe configuration was 44% higher than that for QDSSCs lacking a passivation layer (Table 2 and Figure 6b). The significant increase in the PCE value of the cells indicated the importance of the ZnSe passivation layers in $CuInS_2$/CdSe(3) hybrid-sensitized QDSSCs. We propose that this performance enhancement in hybrid-sensitized QDSSCs treated with ZnSe passivation layers could be attributed to the following properties: (1) ZnSe has a wider band gap (2.7 eV for the bulk material)[58] compared to both CdSe (1.76 eV) and $CuInS_2$ (1.5 eV), which can reduce the recombination of injected electrons with holes in the electrolytes and increase the forward bias current. (2) The lattice mismatch of ZnSe relative to CdSe materials (6.3%)[59] is lower than that of the commonly used shell material ZnS, easily permitting epitaxial growth of the passivation shell on CdSe hybrid-sensitized QDs. However, the large lattice mismatch (ca. 12%) between CdSe and ZnS materials can induce interface strain accumulation, ultimately leading to the formation of relaxing of misfit dislocations[60] and resulting in an increased number of defect states responsible for electron trapping. Additionally, the lattice constants of ZnSe and $CuInS_2$ were also closely matched; the interface created between the two had minimal lattice mismatch (∼2%) between the merging lattices, relieving interfacial strain and reducing the number of interfacial defects.[61,62] In support of this hypothesis, we found that the IPCE curves for the $CuInS_2$/CdSe(3)/ZnSe configuration exhibited significantly enhanced photocurrent densities at wavelengths between 450 and 650 nm, which are higher than those of $CuInS_2$/CdSe(3) hybrid-sensitized QDSSCs with or without ZnS passivation layers (Figure 6b). In comparison with the maximal IPCE value of 50% in $CuInS_2$/CdSe(3) hybrid-sensitized QDSSCs, the maximal IPCE value in $CuInS_2$/CdSe(3) hybrid-sensitized QDSSCs was increased to a maximum value of 80% after the post-treatment of ZnSe passivation layers. The IPCE enhancement probably occurred because ZnSe is an effective passivation layer owing to its minimal lattice mismatch relative to $CuInS_2$ and CdSe hybrid sensitizers, which prevents electron trapping in defect states and renders a higher photocurrent. (3) QD surfaces passivated with ZnSe, as opposed to a ZnS passivation layer, had photogenerated holes in QDs that were effectively scavenged by $S^{2-}/S_x^{2-}$ electrolytes, which is related to anodic photocorrosion.[63,64] Prior work[64] has indicated that $CdSe_xS_{1-x}$ was generated on the top of CdSe and serves as an overcoat layer in the presence of $S^{2-}/S_x^{2-}$ electrolytes. Similarly, the substitution reaction at the interface between ZnSe and $S^{2-}/S_x^{2-}$ electrolytes also formed a $ZnSe_xS_{1-x}$ interface, offering a medium band gap and providing cascade band structures that were advantageous in the separation of excited electrons and holes across the interfacial region.

We use the EDS spectrum in combination with SEM imaging to determine the chemical composition and quantitative analysis of each layer when the corresponding materials are deposited on the $TiO_2$ film. The SEM images show that the samples are closely packed layers composed of a network of spherical particles (Figure S3 (left side) in the Supporting Information). The EDS spectrum in the SEM image (Figure S3 in the Supporting Information) revealed the elemental composition and atomic ratio of each layer, which are very close to the stoichiometric ratio of each layer (i.e., $In_2Se_3$ interfacial buffer layer, $CuInS_2$ sensitized layer, CdSe hybrid-sensitized layer, and ZnSe passivation layer). To understand further and extract the composition information of QDSSCs with the best photovoltaic performance, an XPS analysis was

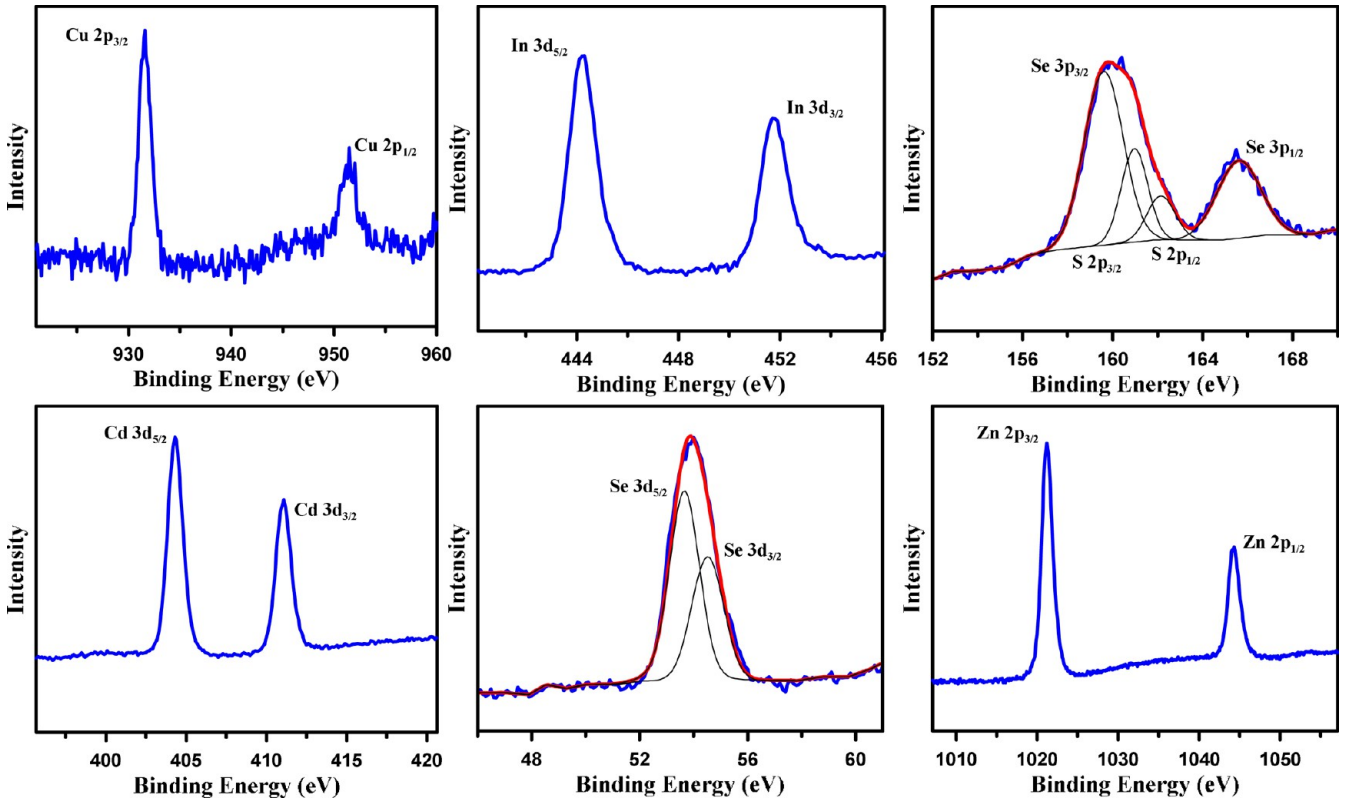


**Figure 7.** High-resolution XPS spectra of a $CuInS_2$/CdSe(3)/ZnSe QDSSC containing an $In_2Se_3$ interfacial buffer layer. Blue lines represent the raw XPS data, black lines are the simulated individual peaks, and red lines are the overall fitted curves.

performed to investigate the valence states of the $CuInS_2$/CdSe(3)/ZnSe configuration containing an $In_2Se_3$ interfacial buffer layer, as shown in Figure 7. The Cu 2p core split into $2p_{3/2}$ (931.50 eV) and $2p_{1/2}$ (951.33 eV) peaks, consistent with the standard separation of 19.83 eV.[65] In addition, the Cu $2p_{3/2}$ satellite peak of Cu(II), which is usually located at 942 eV, did not appear in the spectrum. Therefore, it can be concluded that only monovalent copper exists in the sample. The binding energies of In $3d_{5/2}$ and In $3d_{3/2}$ can be assigned to 444.21 and 451.77 eV, respectively, which is consistent with a valence state of +3 in $CuInS_2$.[66] To fit the S curve, we used the standard S 2p spin−orbit doublet with $\Delta E$ = 1.18 eV between the S $2p_{3/2}$ and S $2p_{1/2}$ components and a fixed intensity ratio of 2:1. The S $2p_{3/2}$ and $2p_{1/2}$ peaks at 160.97 and 162.15 eV, respectively, can be assigned to the S coordinated to Cu and In. Two additional peaks appear at 159.61 and 165.61 eV. These two peaks, with a spin−orbit splitting of 6.0 eV, can be assigned to Se $3p_{3/2}$ and $3p_{1/2}$ orbitals, respectively, which are in good agreement with those values reported elsewhere.[65] Moreover, the spectrum of the Se 3d peak near 54 eV could be deconvoluted into two peaks. The more intense peak at 53.65 eV was attributed to Se $3d_{5/2}$, whereas the weaker peak at 54.51 eV could be assigned to Se $3d_{3/2}$. The Cd 3d peaks appear at binding energies of 404.20 and 411.04 eV and originate from the doublet of Cd $3d_{5/2}$ and Cd $3d_{3/2}$, respectively, suggesting the presence of $Cd^{2+}$. The appearance of Cd $3d_{5/2}$ indicates that Cd prevails in a +2 oxidation state. The Zn 2p peaks are located at 1021.4 and 1044.4 eV with a peak splitting of 23.0 eV, matching well with Zn(II).[67]

**3.4. Electrochemical Impedance Analysis.** To gain further insight into the electron transport and recombination properties of QDSSCs, we utilized EIS under dark conditions at −0.6 V forward bias to investigate the charge-transfer processes in QDSSCs with the same pretreatment of $In_2Se_3$ interfacial buffer layers for the $CuInS_2$/CdSe(3), $CuInS_2$/CdSe(3)/ZnS, and $CuInS_2$/CdSe(3)/ZnSe configurations. Figure 8a shows the Nyquist curves containing two semicircles in the high-frequency and low-frequency regions. These curves represent the recombination resistances ($R$) of the cells. Each semicircle in the Nyquist curves can be modeled with electrical elements (e.g., resistance and constant phase element) to describe interfacial properties, internal resistance, and charge-transfer kinetics. The impedance spectra were analyzed by Nova software using an equivalent circuit consisting of (1) a series of resistances corresponding with transport resistances of ITO and all resistances outside of the cell ($R_s$; starting point of the first semicircle), (2) recombination resistances at the counter electrode/electrolyte interface ($R_1$; small semicircle at high frequency) parallel to the constant phase element of capacitance corresponding to $R_1$ (CPE1), and (3) recombination resistances at the $TiO_2$/QDs/electrolyte interface ($R_2$; large semicircle at low frequency) parallel to the constant phase element of capacitance corresponding to $R_2$ (CPE2), as represented in the inset of the Figure 8a. By fitting the experimental data with the inset equivalent circuit simulation, resistance values ($R_s$, $R_1$, and $R_2$) could be obtained (Table 3). We observed that the $R_s$ values of all cells were similar because of the utilization of identical counter electrodes (Pt/ITO glass). The value of $R_1$ resulted from the recombination resistance at the counter electrode/electrolyte solution interface. We propose that the increase in $R_1$ could be attributed to the property alternation of polysulfide electrolytes under identical platinum counter electrodes in our device. Because $R_1$ of the $CuInS_2$/CdSe(3) configuration (90.5 Ω) was smaller than that


dx.doi.org/10.1021/am402547e | ACS Appl. Mater. Interfaces 2013, 5, 8740−8752

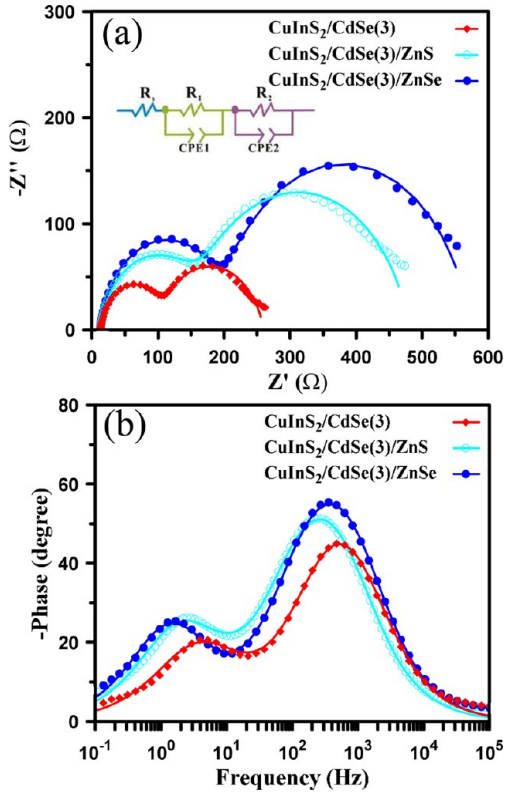


**Figure 8.** (a) Nyquist and (b) Bode plots from impedance spectra of a QDSSC fabricated with different sensitization conditions. The inset of panel a shows the corresponding equivalent circuit model simulated to fit the impedance spectra. The symbols and solid lines are the experimental and fitted results, respectively, according to the inset equivalent circuit model.

**Table 3. EIS Parameters Determined by Fitting the Impedance Spectra of QDSSC Fabricated under Different Sensitization Conditions**

| sample | $R_s$ (Ω) | $R_1$ (Ω) | $R_2$ (Ω) | $\tau_r$ (ms) |
|---|---|---|---|---|
| $CuInS_2$/CdSe(3) | 13.1 | 90.5 | 157 | 40.7 |
| $CuInS_2$/CdSe(3)/ZnS | 12.9 | 143 | 325 | 64.3 |
| $CuInS_2$/CdSe(3)/ZnSe | 12.3 | 183 | 378 | 94.9 |

of the $CuInS_2$/CdSe(3)/ZnS (143 Ω) and $CuInS_2$/CdSe(3)/ZnSe (183 Ω) configurations, our results suggest that electron injection at the counter electrode/electrolyte solution interface was more efficient in the presence of a ZnS or ZnSe passivation layer, preventing undesirable leakage from the $CuInS_2$ QDs to the electrolytes. The $R_2$ value for the $CuInS_2$/CdSe(3)/ZnS configuration, 325 Ω, was found to be increased from that for the $CuInS_2$/CdSe(3) configuration, 157 Ω. This result suggests that the $CuInS_2$/CdSe(3)/ZnS configuration supports better electron transport in the photoanode by suppressing the recombination when the ZnS layer passivates on the surface of $CuInS_2$ and CdSe QDs. Furthermore, the $CuInS_2$/CdSe(3)/ZnSe configuration had the highest $R_2$ (378 Ω), highlighting the crucial role of ZnSe treatment in effectively passivating the surface of $CuInS_2$ and CdSe QDs. As mentioned previously, the large lattice mismatch between CdSe and ZnS materials would result in higher numbers of defect or trap states responsible for recombining electrons. This resulting ZnSe passivation layer could effectively decrease electron recombination, leading to significantly enhanced electron transfer, improved $J_{SC}$ values, and superior photovoltaic performance.

The corresponding Bode phase plots for cells with different configurations are shown in Figure 8b. Electron lifetimes ($\tau_r$) can be estimated according to the following equation

$$\tau_r = 1/(2\pi f_{max}) \quad (1)$$

where $f_{max}$ is the maximum frequency of the middle-frequency peak in the Bode plot. We found that $\tau_r$ was 40.7 ms for the $CuInS_2$/CdSe(3) configuration and 64.3 ms for the $CuInS_2$/CdSe(3)/ZnS configuration (Table 3). A higher value of $\tau_r$ suggests that electrons have a longer lifetime and are effectively transferred, resulting in higher photocurrents and PCEs for QDSSCs. This result suggests that there was more effective suppression of back reactions for electrons injected with electrolytes, leading to the capture of more electrons in QDSSCs that contained a ZnS passivation layer. Furthermore, $\tau_r$ values for the $CuInS_2$/CdSe(3)/ZnSe configuration had the highest value of 94.9 ms, indicating that the ZnSe layer effectively passivated the surface states of the $CuInS_2$ and CdSe QDs and hence reduced the recombination by the surface states of the QDs.

Figure 9a shows a plot of the fitted recombination resistance ($R_2$) and the chemical capacitance ($C_{\mu 2}$) as a function of the

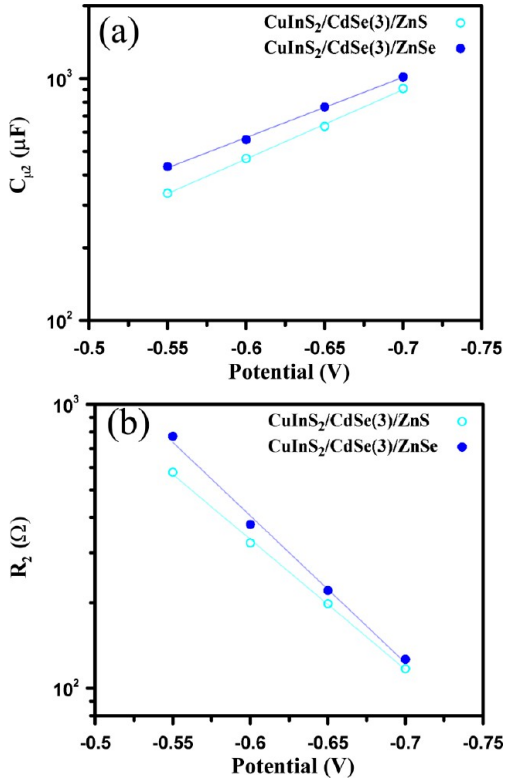


**Figure 9.** Fitting results for (a) the chemical capacitance ($C_{\mu 2}$) and (b) the recombination resistance ($R_2$) as functions of applied voltage in the dark.

bias voltage. As shown, the logarithmic plots reveal the almost linear dependence of $R_2$ and $C_{\mu 2}$ as a function of the applied potential for the photoanodes. It was shown that chemical capacitance is described by the expression[68]


dx.doi.org/10.1021/am402547e | ACS Appl. Mater. Interfaces 2013, 5, 8740−8752

$$C_{\mu 2} = C_{\mu 0} \exp\left( - \alpha \frac{qV}{k_B T} \right) \quad (2)$$

with

$$C_{\mu 0} = L(1 - p)\, \alpha \frac{q^2 N_t}{k_B T} \exp\left[ \left( - \alpha \frac{E_{redox} - E_c}{k_B T} \right) \right] \quad (3)$$

where $C_{\mu 0}$ is a constant, $\alpha$ is a constant related to the distribution of the electronic states below the conduction band, $q$ is the elementary charge, $k_B$ is the Boltzmann constant, $V$ is the applied voltage, $T$ is the temperature, $L$ represents the film thickness, $p$ is the porosity of the film, $E_{redox}$ is the redox potential of the electrolyte, $E_c$ is the position of the conduction band edge, and $N_t$ is the total number of trap states below the conduction band. $C_{\mu 2}$ denotes the degree of electron accumulation in the photoanode.[69−71] In terms of the slope of $C_{\mu 2}$, $\alpha$ is calculated to be 0.17 for the $CuInS_2$/CdSe(3)/ZnS configuration and 0.15 for the $CuInS_2$/CdSe(3)/ZnSe configuration, which is in agreement with the reported $1 > \alpha > 0$, indicating an exponential distribution of traps below the conduction band edge.[72,73] The trend observed in Figure 9a indicates that the $C_{\mu 2}$ of the $CuInS_2$/CdSe(3)/ZnS configuration was higher than that of the $CuInS_2$/CdSe(3)/ZnSe configuration. This suggests that more electrons were accumulated in the conduction band of $TiO_2$ because the ZnS semiconductor possesses wider band gaps than the ZnSe semiconductors, effectively preventing charge leakage from the QD to the electrolyte. As a result, the more negative shift in the conduction band potential for $TiO_2$ was beneficial to the increase in the $V_{OC}$ for the $CuInS_2$/CdSe(3)/ZnS-based QDSSC, as shown in Table 2.

Under dark conditions, $R_2$ followed a characteristic exponential rise with the increase in the forward bias in the QDSSC devices, which is consistent with the expression

$$R_2 = R_0 \exp\left( - \beta \frac{qV}{k_B T} \right) \quad (4)$$

where $R_0$ is a constant and $\beta$ is the transfer coefficient. This plot demonstrates a much stronger forward bias dependence for the presence of ZnSe passivation in QDSSCs. The $R_2$ values for the electrolytes are in the order $CuInS_2$/CdSe(3)/ZnSe > $CuInS_2$/CdSe(3)/ZnS in Figure 9b.

The higher $R_2$ reveals that the ZnSe passivation layer on the $TiO_2$ electrode effectively suppressed the number of recombination centers and limited the charge losses, as discussed above. From the fitting of $R_2$ versus $V$ as shown in Figure 9b, the $\beta$ values of $CuInS_2$/CdSe(3)/ZnSe and $CuInS_2$/CdSe(3)/ZnS were calculated to be 0.31 and 0.27, respectively. As mentioned previously,[1,74] a larger $\beta$ value is associated with a shallower distribution of the defect states and a better FF at a given $V_{OC}$. In other words, the influence of the transfer coefficient on the FF of a QDSSC is indicative of the preparation of a $TiO_2$ film with an optimum surface state distribution. This is consistent with results found in the $J-V$ curves in which the FF was 36.9% for $CuInS_2$/CdSe(3)/ZnS and 46.5% for $CuInS_2$/CdSe(3)/ZnSe, as shown in Table 2.

## 4. CONCLUSIONS

We developed a multilayered QDSSC with a distinct architecture in an effort to improve the PCE of photovoltaic cells. We also investigated the impact of interfacial layers, including buffer layers, hybrid-sensitized layers, and passivation layers, on the photovoltaic performance of $CuInS_2$-based QDSSCs. Both $J_{SC}$ and $V_{OC}$ were improved in $CuInS_2$-based QDSSCs in the presence of interfacial buffer layers because of the proper band alignment across the heterointerface and because of the negative band edge movement of $TiO_2$. We found that $CuInS_2$-based QDSSCs that contained $In_2Se_3$ interfacial buffer layers exhibited the best performance compared to pristine $CuInS_2$-based QDSSCs that lacked interfacial buffer layers. In addition, the subsequent introduction of an alternative sensitizer into $CuInS_2$-based QDSSCs provided complementary light harvest. In particular, $CuInS_2$/CdSe hybrid-sensitized QDSSCs offered a combined synergetic effect of enhanced light-harvesting capacity and a favorable stepwise cascade, resulting in an improvement in PCE by a factor of 1.3 compared to the $CuInS_2$-based QDSSCs. We also determined that the highest recombination resistances and longest electron lifetimes occurred for the $CuInS_2$/CdSe(3)/ZnSe configuration, suggesting that ZnSe treatments played a crucial role in effectively passivating the surface of $CuInS_2$ and CdSe QDs and suppressing electron recombination. Most significantly, $CuInS_2$/CdSe hybrid-sensitized QDSSCs created through the combination of $In_2Se_3$ interfacial buffers and ZnSe passivation layers had the highest $J_{SC}$, $V_{OC}$, FF, and PCE values. It is believed that this proof of concept can also be used to fabricate different types of I-III-VI-based QDSSCs with enhanced performance.

## ■ ASSOCIATED CONTENT

### Supporting Information

Average PCE of $CuInS_2$-based QDSSCs containing different interfacial buffer layers of metal chalcogenide; EDS spectra of $CuInS_2$/CdS(3) and $CuInS_2$/CdSe(3) hybrids sensitized on TiO2 photoelectrode; and SEM images and the corresponding EDS spectra of the QDSSCs sequentially deposited by an $In_2Se_3$ interfacial buffer-layer, a $CuInS_2$-sensitized layer, a CdSe hybrid sensitized layer, and a ZnSe passivation layer. This material is available free of charge via the Internet at http://pubs.acs.org.

## ■ AUTHOR INFORMATION

### Corresponding Author

*E-mail: jychang@mail.ntust.edu.tw. Tel: +886-2-27303636. Fax: +886-2-27376644.

### Notes

The authors declare no competing financial interest.

## ■ ACKNOWLEDGMENTS

The authors thank the National Science Council of the Republic of China for financially supporting this research under contract no. NSC 102-2628-M-011-001-MY3.

## ■ REFERENCES

(1) Grätzel, M. *Acc. Chem. Res.* **2009**, *42*, 1788−1798.
(2) Yella, A.; Lee, H.-W.; Tsao, H. N.; Yi, C.; Chandiran, A. K.; Nazeeruddin, M.; Diau, E. W.-G.; Yeh, C.-Y.; Zakeeruddin, S. M.; Grätzel, M. *Science* **2011**, *334*, 629−634.
(3) Snatra, P. K.; Kamat, P. V. *J. Am. Chem. Soc.* **2012**, *134*, 2508−2511.
(4) Beard, M. C.; Midgett, A. G.; Hanna, M. C.; Luther, J. M.; Hughes, B. K.; Nozik, A. J. *Nano Lett.* **2010**, *10*, 3019−3027.
(5) Pijpers, J. J. H.; Ulbricht, R.; Tielrooij, K. J.; Osherov, A.; Golan, Y.; Delerue, C.; Allan, G.; Bonn, M. *Nat. Phys.* **2009**, *5*, 811−814.

(6) McGuire, J. A.; Sykora, M.; Joo, J.; Pietryga, J. M.; Klimov, V. I. *Nano Lett.* **2010**, *10*, 2049−2057.
(7) Fuke, N.; Hoch, L. B.; Koposov, A. Y.; Manner, V. W.; Werder, D. J.; Fukui, A.; Koide, N.; Katayama, H.; Sykora, M. *ACS Nano* **2010**, *4*, 6377−6386.
(8) Korte, L.; Schmidt, M. *J. Non-Cryst. Solids* **2008**, *354*, 2138−2143.
(9) Green, A. M.; Emery, K.; Hishikawa, Y.; Warta, W. *Prog. Photovoltaics* **2008**, *16*, 61−67.
(10) Bhattacharya, R. N.; Contreras, M. A.; Teeter, G. *Jpn. J. Appl. Phys.* **2004**, *43*, L1475−L1476.
(11) Robel, I.; Subramanian, V.; Kuno, M.; Kamat, P. V. *J. Am. Chem. Soc.* **2006**, *128*, 2385−2393.
(12) Qian, S.; Wang, C.; Liu, W.; Zhu, Y.; Yao, W.; Lu, X. *J. Mater. Chem.* **2011**, *21*, 4945−4952.
(13) Barea, E. M.; Shalom, M.; Giménez, S.; Hod, I.; Mora-Seró, I.; Zaban, A.; Bisquert, J. *J. Am. Chem. Soc.* **2010**, *132*, 6834−6839.
(14) Shalom, M.; Ruhle, S.; Hod, I.; Yahav, S.; Zaban, A. *J. Am. Chem. Soc.* **2009**, *131*, 9876−9877.
(15) Mora-Seró, I.; Bisquert, J. *J. Phys. Chem. Lett.* **2010**, *1*, 3046−3052.
(16) Samadpour, M.; Boix, P. P.; Giménez, S.; Zad, A. I.; Taghavinia, N.; Mora-Seró, I.; Bisquert, J. *J. Phys. Chem. C* **2011**, *115*, 14400−14407.
(17) Im, S. H.; Lee, Y. H.; Seok, S. I.; Kim, S. W.; Kim, S.-W. *Langmuir* **2010**, *26*, 18576−18580.
(18) Xu, G.; Ji, S.; Miao, C.; Liu, G.; Ye, C. *J. Mater. Chem.* **2012**, *22*, 4890−4896.
(19) Hu, X.; Zhang, Q.; Huang, X.; Li, D.; Luo, Y.; Meng, Q. *J. Mater. Chem.* **2011**, *21*, 15903−15905.
(20) Chang, J.-Y.; Su, L.-F.; Li, C.-H.; Chang, C.-C.; Lin, J.-M. *Chem. Commun.* **2012**, *48*, 4848−4850.
(21) Lin, K.-H.; Chung, C.-Y.; Lee, Y.-Y.; Li, F.-C.; Chang, Y.-M.; Lu, I.-P.; Chou, S.-C.; Lee, Y. L. *J. Phys. Chem. C* **2012**, *116*, 1550−1555.
(22) Lee, Y.-L.; Lo, Y.-S. *Adv. Funct. Mater.* **2009**, *19*, 604−609.
(23) Lee, H. J.; Bang, J.; Park, J.; Kim, S.; Park, S.-M. *Chem. Mater.* **2010**, *22*, 5636−5643.
(24) Hossain, M. A.; Jennings, J. R.; Koh, Z. Y.; Wang, Q. *ACS Nano* **2011**, *5*, 3172−3181.
(25) Chang, S.; Fu, W.; Yang, H.; Zhang, L.; Ma, J.; Zhao, H.; Sun, M.; Yang, L. *J. Phys. Chem. C* **2012**, *116*, 2615−2621.
(26) Tian, J.; Zhang, Q.; Zhang, L.; Gao, R.; Shen, L.; Zhang, S.; Qu, X.; Cao, G. *Nanoscale* **2013**, *5*, 936−943.
(27) Yang, S.-M.; Huang, C.-H.; Zhai, J.; Wang, Z.-S.; Jiang, L. *J. Mater. Chem.* **2002**, *12*, 1459−1464.
(28) Diguna, L. J.; Shen, Q.; Kobayashi, J.; Toyoda, T. *Appl. Phys. Lett.* **2007**, *91*, 023116-1−023116-3.
(29) Shen, Q.; Kobayashi, J.; Diguna, L. J.; Toyoda, T. *J. Appl. Phys.* **2008**, *103*, 084304-1−084304-5.
(30) Lee, Y.-L.; Huang, B.-M.; Chien, H.-T. *Chem. Mater.* **2008**, *20*, 6903−6905.
(31) Tubtimtae, A.; Wu, K.-L.; Tung, H.-Y.; Lee, M.-W.; Wang, G. J. *Electrochem. Commun.* **2010**, *12*, 1158−1160.
(32) Salant, A.; Shalom, M.; Hod, I.; Faust, A.; Zaban, A.; Banin, U. *ACS Nano* **2010**, *4*, 5962−5968.
(33) Tubtimtae, A.; Lee, M.-W.; Wang, G.-J. *J. Power Sources* **2011**, *196*, 6603−6608.
(34) Guijarro, N.; Campiña, J. M.; Shen, Q.; Toyoda, T.; Lana-Villarreal, T.; Gómez, R. *Phys. Chem. Chem. Phys.* **2011**, *13*, 12024−12032.
(35) Alonso, M. I.; Wakita, K.; Pascual, J.; Garriga, M.; Yamamoto, N. *Phys. Rev. B* **2001**, *63*, 075203.
(36) Lee, H.; Wang, M.; Chan, P.; Gamelin, D. R.; Zakeeruddin, S. M.; Grätzel, M.; Nazeeruddin, M. K. *Nano Lett.* **2009**, *9*, 4221−4227.
(37) Naghavi, N.; Abou-Ras, D.; Allsop, N.; Barreau, N.; Bücheler, S.; Ennaoui, A.; Fischer, C.-H.; Guillen, C.; Hariskos, D.; Herrero, J.; Klenk, R.; Kushiya, K.; Lincot, D.; Menner, R.; Nakada, T.; Platzer-Björkman, C.; Spiering, S.; Tiwari, A. N.; Törndahl, T. *Prog. Photovoltaics* **2010**, *18*, 411−433.
(38) Ahn, B. T.; Larina, L.; Kim, K. H.; Ahn, S. J. *Pure Appl. Chem.* **2008**, *80*, 2091−2102.
(39) Ramanathan, K.; Contreras, M. A.; Perkins, C. L.; Asher, S.; Hasoon, F. S.; Keane, J.; Young, D.; Romero, M.; Metzger, W.; Noufi, R.; Ward, J.; Duda, A. *Prog. Photovoltaics* **2003**, *11*, 225−230.
(40) Loef, R.; Schooman, J.; Goossens, A. *J. Appl. Phys.* **2007**, *102*, 024512-1−024512-6.
(41) Wienke, J.; Krunks, M.; Lenzmann, F. *Semicond. Sci. Technol.* **2003**, *18*, 876−880.
(42) Robinson, R. D.; Sadtler, B.; Demchenko, D. O.; Erdonmez, C. K.; Wang, L.-W.; Alivisatos, A. P. *Science* **2007**, *317*, 355−358.
(43) Han, W.; Yi, L.; Zhao, N.; Tang, A.; Gao, M.; Tang, Z. *J. Am. Chem. Soc.* **2008**, *130*, 13152−13161.
(44) Luther, J. M.; Zheng, H.; Sadtler, B.; Alivisatos, A. P. *J. Am. Chem. Soc.* **2009**, *131*, 16851−16857.
(45) Jain, P. K.; Amirav, L.; Aloni, S.; Alivisatos, A. P. *J. Am. Chem. Soc.* **2010**, *132*, 9997−9999.
(46) Chang, J.-Y.; Cheng, C.-Y. *Chem. Commun.* **2011**, *47*, 9089−9091.
(47) Casavola, M.; van Husi, M. A.; Bals, S.; Lambert, K.; Hens, Z.; Vanmaekelbergh, D. *Chem. Mater.* **2012**, *24*, 294−302.
(48) Julien, C.; Hatzikraniotis, E.; Kambas, K. *Phys. Status Solidi A* **1986**, *97*, 579−585.
(49) Zhai, T.; Ma, Y.; Li, L.; Fang, X.; Liao, M.; Koide, Y.; Yao, J.; Bando, Y.; Golberg, D. *J. Mater. Chem.* **2010**, *20*, 6630−6637.
(50) Tian, J.; Gao, R.; Zhang, Q.; Zhang, S.; Li, Y.; Lan, J.; Qu, X.; Cao, G. *J. Phys. Chem. C* **2012**, *116*, 18655−18662.
(51) Zhang, Q.; Guo, X.; Huang, X.; Huang, S.; Li, D.; Luo, Y.; Shen, Q.; Toyoda, T.; Meng, Q. *Phys. Chem. Chem. Phys.* **2011**, *13*, 4659−4667.
(52) Fan, S.-Q.; Fang, B.; Kim, J. H.; Jeong, B.; Kim, C.; Yu, J.-S.; Ko, J. *Langmuir* **2010**, *26*, 13644−13649.
(53) Chang, J. A.; Rhee, J. H.; Im, S. H.; Lee, Y. H.; Kim, H.-J.; Seok, S. I.; Nazeeruddin, M. K.; Grätzel, M. *Nano Lett.* **2010**, *10*, 2609−2612.
(54) Yu, P.; Zhu, K.; Norman, A. G.; Ferrere, S.; Frank, A. J.; Nozik, A. J. *J. Phys. Chem. B* **2006**, *110*, 25451−25454.
(55) Lee, Y.-L.; Chi, C.-F.; Liau, S.-Y. *Chem. Mater.* **2010**, *22*, 922−927.
(56) Buhbut, S.; Itzhakov, S.; Tauber, E.; Shalom, M.; Hod, I.; Geiger, T.; Garini, Y.; Oron, D.; Zaban, A. *ACS Nano* **2010**, *4*, 1293−1298.
(57) Jung, M.-H.; Kang, M. G. *J. Mater. Chem.* **2011**, *21*, 2694−2700.
(58) Wang, M.; Fei, G. T.; Zhang, Y. G.; Kong, M. G.; Zhang, L. D. *Adv. Mater.* **2007**, *19*, 4491−4494.
(59) Reiss, P.; Bleuse, J.; Pron, A. *Nano Lett.* **2002**, *2*, 781−784.
(60) Dabbousi, B. O.; Rodriguez-Viejo, J.; Mikulec, F. V.; Heine, J. R.; Mattoussi, H.; Ober, R.; Jensen, K. F.; Bawendi, M. G. *J. Phys. Chem. B* **1997**, *101*, 9463−9475.
(61) Hofmann, A.; Pettenkofer, C. *Appl. Phys. Lett.* **2011**, *98*, 113503-1−113503-3.
(62) Wei, S. -H.; Zunger, A. *J. Appl. Phys.* **1995**, *78*, 3846−3856.
(63) Bang, J. H.; Kamat, P. V. *ACS Nano* **2009**, *3*, 1467−1476.
(64) Chakrapani, V.; Baker, D.; Kamat, P. V. *J. Am. Chem. Soc.* **2011**, *133*, 9607−9615.
(65) Chiang, M.-Y.; Chang, S.-H.; Chen, C.-Y.; Yuan, F.-W.; Tuan, H.-Y. *J. Phys. Chem. C* **2011**, *115*, 1592−1599.
(66) Zhong, H.; Zhou, Y.; Ye, M.; He, Y.; Ye, J.; He, C.; Yang, C.; Li, Y. *Chem. Mater.* **2008**, *20*, 6434−6443.
(67) Ou, K.-L.; Fan, J.-C.; Chen, J.-K.; Huang, C.-C.; Chen, L.-Y.; Ho, J.-H.; Chang, J.-Y. *J. Mater. Chem.* **2012**, *22*, 14667−14673.
(68) Raga, S. R.; Barea, E. M.; Fabregat-Santiago, F. *J. Phys. Chem. Lett.* **2012**, *3*, 1629−1634.
(69) Fabregat-Santiago, F.; Bisquert, J.; Palomares, E.; Otero, L.; Kuang, D.; Zakeeruddin, S. M.; Grätzel, M. *J. Phys. Chem. C* **2007**, *111*, 6550−6560.
(70) Fabregat-Santiago, F.; Garcia-Belmonte, G.; Mora-Seró, I.; Bisquert, J. *Phys. Chem. Chem. Phys.* **2011**, *13*, 9083−9118.

(71) Kim, J.-Y.; Kim, J. Y.; Lee, D.-K.; Kim, B.; Kim, H.; Ko, M. J. *J. Phys. Chem. C* **2012**, *116*, 22759−22766.
(72) Shi, J.; Peng, B.; Pei, J.; Peng, S.; Chen, J. *J. Power Sources* **2009**, *193*, 878−884.
(73) Zhang, Z.; Zakeeruddin, S. M.; O'Regan, B. C.; Humphry-Baker, R.; Grätzel, M. *J. Phys. Chem. B* **2005**, *109*, 21818−21824.
(74) Wang, Q.; Ito, S.; Grätzel, M.; Fabregat-Santiago, F.; Mora-Seró, I.; Bisquert, J.; Bessho, T.; Imai, H. *J. Phys. Chem. B* **2006**, *110*, 25210−25221.